Cosmic Muon Physics with the MINOS Far Detector

S.L.Mufson & B.J.Rebel

July 1, 2005

Abstract

We did stuff. We looked for things. We spent a lot of time on stuff most consider worthless. But we don't care. It's fun to be a scientist so we had some fun. As bungee-jumping out of a 747 is fun.

Contents

1 Introduction

We undertook our study of cosmic ray muon distributions in the MINOS far detector primarily to understand how well we reconstruct muon charge sign. This work was to go in two steps. First, we would verify that the distributions of cosmics without charge sign discrimination measured by the MINOS far detector were consistent with those previously measured at the Soudan mine [1]. Second, we would characterize our cosmic distributions with charge sign discrimination and compare our results with theory [2]. Our expectation was that the detector's physical properties, alignment, and magnetic field map were well enough characterized that muon charge sign determination would be reasonably straightforward for tracks having sufficient curvature, typically those with momentum less than 30-40 GeV/c. We expected these studies, for us a necessary step toward reliable, quantitative measurements of the atmospheric neutrino-induced muons, to be routine. In addition to their value as calibrations of the MINOS far detector, these distributions have intrinsic scientific value. They yield the muon charge ratio for a surface distribution of cosmic muons in an unexplored energy range. They also provide the data needed to search for possible interesting effects in the seasonal variations, vertical intensity, and moon shadow as a function of charge sign. Finally, these measurements result in a clean, charge-separated muon data sample that could be used to investigate other interesting physics topics, such as the shadow of the sun in cosmic muons.

In this note we describe the current state of our understanding of the cosmic ray muon distributions in the MINOS far detector.

2 Data Samples: Cosmic Muons and Simulated Cosmic Muons

The data we analyzed start at run 17,567 (July 17, 2003) and end at run 31,356 (April 30, 2005). During this period, the detector had two different magnetic field orientations. One orientation, "Forward Field", focuses μ^- from the south into the detector and is the default orientation for intitial MINOS data-taking with the NuMI beam from Fermilab. The second orientation, "Reverse Field", focuses μ^+ from the south into the detector. There were 304.17 live days of forward field running and 163.72 live days of reverse field running.

In our studies, we analyzed three samples of cosmic muons using the MINOS Standard Reconstruction (SR) software. We analyzed two samples of observed cosmic muons, one in the forward field ("DF" – data forward) and one in the reverse field ("DR" – data reverse). There were 14,705,956 events in the DF sample and 7,734,841 events in the DR sample. In addition, we processed a simulated data sample muons of Monte Carlo-generated muons ("MC" – Monte Carlo) using the same analysis procedures; these MC muons were generated with the standard MINOS cosmics generator. There were 2,812,704 events in the MC sample.

2.1 Pre-Analysis Event Cuts and Run Rate Cuts

As described below, several pre-analysis event cuts and run rate cuts were applied to the three data sets. The effects of these cuts on the three data samples are given in Table 1.

1. "deMuxing Cut" – an event was excluded if it failed the deMuxing algorithm. The SR deMuxing algorithm is described in detail in [3]. There were significantly more deMuxing failures in the DF data sample than the DR sample.

2. "multiples cut" – those events successfully passing the deMuxing procedure were then scanned for potential tracks and the results of the track finding algorithm were then passed on to the track fitter. Both the track-finding and track-fitting algorithms we used are those in SR. In the MC data sample, some single events (for example, those passing through the coil hole) were reconstructed as multiples since there are no multiples built into the MC sample.

   An event was excluded if there were multiple tracks reconstructed in it.

3. "coil cut" – an event was excluded if the coil was either off or the field was in an unknown state

   Although there are significantly more deMuxing failures in the DF sample, there is a compensating number of events cut from the DR sample with the coil cut. After these three cuts, the fraction remaining in the DF and DR samples are approximately the same.

4. "run rates $> 3\sigma$ from the mean" – a entire run was excluded from further analysis if the rate of single track events was $> 3\sigma$ from mean of all runs in that data set. This cut is based on the expectation that changes in the cosmic ray flux at TeV energies should be small; this cut removes rates that are $> 8\%$ from the mean. The cut was applied to the total rate in the run, without charge separation. The cut is shown superposed on the distribution of run rates in the top panel of Figs.1a and 1b for the DF and DR samples, respectively. How this cut affects the run rate distributions for μ^+ and μ^- is shown in the bottom panels of these figures. In Figure 2, we show the rate/day as a function of Julian day number from the beginning of data taking with the full detector-coil on. In the top panel, the rates are shown before the run rate cut is applied; in the lower panel, the rates are shown after the cut is applied. Clearly a significant number of the runs cut are from the period near the start of the data-taking.

After cuts, there were 10,338,287 events in the DF sample; 5,592,290 events in the DR sample; and 2,557,999 events in the MC sample.

Table 1. Effect of Pre-Analysis and Run Rate Cuts Applied to Cosmic Muon Data Samples

	Fraction Remaining		
cut	**DF**†	**DR**†	**MC**†
0. no cuts	1.0	1.0	1.0
1. deMuxing cut	0.811	0.902	0.925
2. multiples cut	0.779	0.867	0.913
3. coil cut	0.720	0.732	0.913
4. run rates $> 3\sigma$ from mean	0.703	0.722	0.913

† DF = cosmic data set, forward field; DR = cosmic data set, reverse field; MC = Monte Carlo data set

Table 1 shows that pre-analysis and run cuts affect the DF and DR samples similarly. The differences in the MC sample are due to the fact that there are no multiples in the MC event generation and the coil is always 'on'. In addition, since the MC events were not generated on a run-by-run basis, there are no run rate losses.

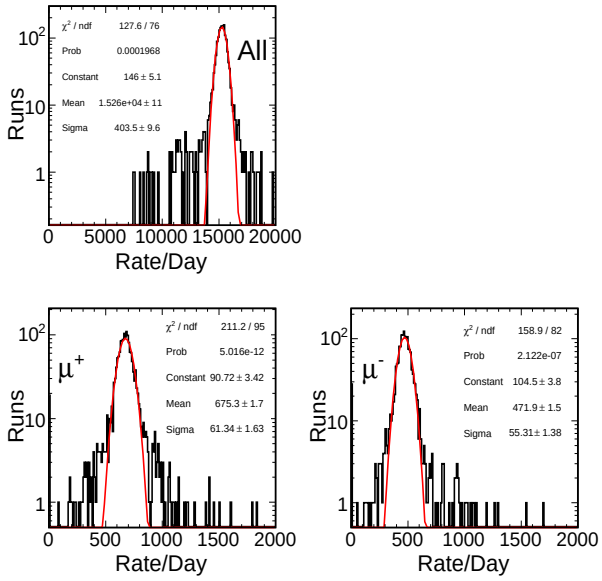

Figure 1a. Run rates for DF data sample without charge separation is shown in the top plot. The 3σ cut as applied to this distribution is superposed. How this cut affects the μ^+ and μ^- distributions is shown in the two lower plots.

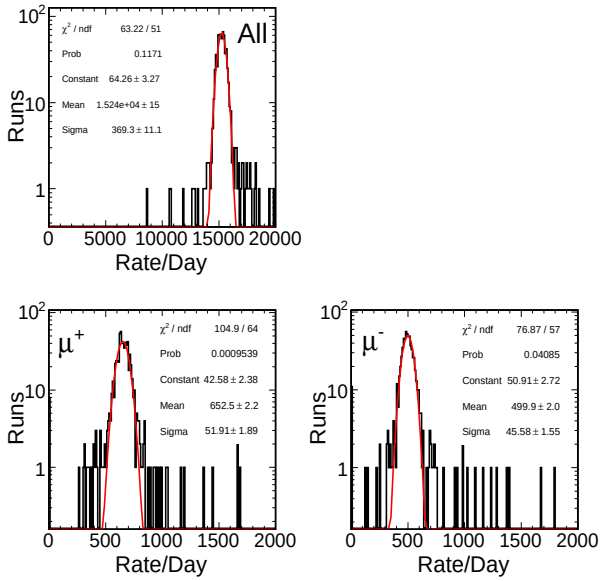

Figure 1b. Same as Fig.1a for the DR data sample.

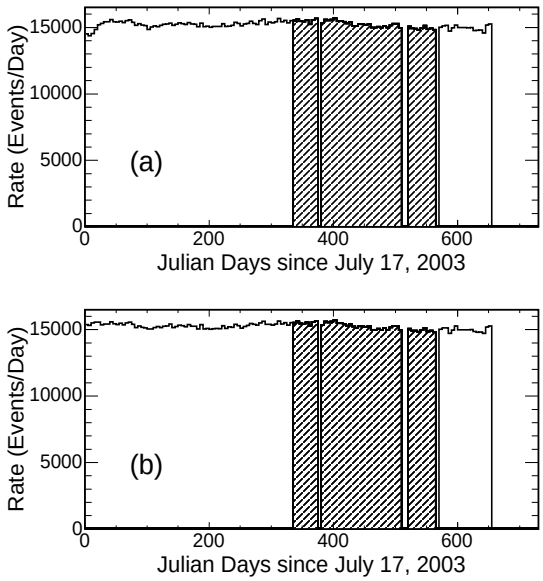

Figure 2. Muon rates per day as a function of Julian day number from the start of data taking with the full detector-coil on are shown in the top plot. The effect of the rate cuts are shown in the lower plot. The shaded area shows the period of reverse field running.

2.2 Analysis Cuts

The following cuts were applied to the single reconstructed track in the selected events. The effect of these cuts on the three data samples is given in Table 2.

1. "plane cut" – the track was excluded if it crossed < 20 planes
2. "length cut" – the track was excluded if its total path length in the detector was < 2.0 m
3. "fiducial cut" – the track was excluded if either the (x,y) coordinates of its vertex were farther than 50cm from an outside surface of the detector or the (x,y) coordinates of the its endpoint were more than 50 cm outside the detector.
4. "tracking quality cuts" – there are three components to the fit quality cuts:
   (a) the track was excluded if it failed the track-fitting algorithm's internal consistency checks.
   (b) the track was excluded if $\chi^2_{fitter}/ndf > 2.0$ for the fit. The distribution used to determine the empirical cut value used is shown in Fig.3.
   (c) the number of planes used in each view was required to be approximately the same; this requirement removes events in which the track fitting algorithm stops tracking planes in one view. The asymmetry is quantified by $\mathcal{A}$,
   $$\mathcal{A} = \frac{\mathcal{N}_\mathcal{U} - \mathcal{N}_\mathcal{V}}{\mathcal{N}_\mathcal{U} + \mathcal{N}_\mathcal{V}},$$
   where $\mathcal{N}_\mathcal{U}(\mathcal{N}_\mathcal{V})$ is the number of planes in the $\mathcal{U}(\mathcal{V})$ view.
   The track was excluded if $\mathcal{A} \geq 0.11$, an empirical cut value that corresponds to more than 20% of the total planes not having information in both views.
5. "muon-like cut" – the track was excluded if it was not classified as a muon. This cut was meant to exclude tracks dominated by electromagnetic or hadronic showers. Our simple muon classification requires that $\geq 40\%$ of the total signal and $\geq 40\%$ of the total planes hit be used in the track OR the track be at least 4.0 m long OR the track cross at least 60 planes. Scanning shows that these criteria are sufficient to pick out a cosmic muon track.
6. "timing quality cuts" – there are three components to the timing quality cuts:

(a) the track was excluded if $\leq 50\%$ of the strips had signals read out on both ends. Since strips with signal on only one end often correspond to noise hits, these strips also degrade the quality of the timing of the track.

(b) the track was excluded if $\chi^2_{dt/dy}/ndf < 3.0$ for its fit to dt/dy, where t is the time for each track point relative to the time of the vertex hit and y is the vertical position of the track point in the MINOS detector. The $\chi^2_{dt/dy}/ndf$ distribution and the value chosen for this cut are shown in Fig.4.

(c) the track was excluded if its timing information indicated that the track was downward(upward)-going but its fit trajectory at the vertex showed the track to be upward(downward)-going.

7. "charge-sign quality cuts" – there are three components to the charge-sign quality cuts:

   (a) "minimum-information-in-the-inner-part-of-the-detector-where-we-know-things cut (MIITIPOTDC)" – We were motivated to make this cut by Jeff Nelson who pointed out that the B field vector in the outer part of the detector, where the steel is not saturated, can have significant fractional errors. Since the Kalman filter in SR weights track points equally in its determination of (q/p) = charge sign/momentum and track direction, significant systematic errors in the fit parameters might be introduced by the equal-weighted outer track points. Instead of deweighting the outer track points, we instead demanded that the track fit be dominated by information in the better understood inner regions of the detector. We used the following cut.

   The track was excluded if fewer than 60 planes of information on its track were within 3.5 meters of the detector center.

   The rationale for this cut is explained in Fig.5. In this figure we have plotted the muon charge ratio, N_{μ^+}/N_{μ^-} for the DF data sets as a function of fit momentum for track fit information restricted to radii of 3.0m, 3.5m, and 4.0m from the detector center. For each plot, the number of planes of information required has been varied from 0-60 planes. There is a large and unexpected bump in this distribution that peaks in the neighborhood of 40-50 GeV which first decreases significantly as the fraction of the track information in the well-characterized inner part of the detector increases as quantified by the number of track points in the inner region of the detector. Our expectation was that if this were a real physical effect, then it would not disappear as the quality of the fit information improved. As is clear from Fig.5, this is not the case. Our conclusion is that this behavior is the result of a systematic effect and does not have a real physical cause. To define the cut we chose those parameters that flattened out the bump while keeping the greatest number of

events. In our long search for the causes of the peculiarities we saw in the cosmic ray distributions over the years, we actually made this cut last. But technically it goes here.

We agree with those who claim that this cut might not be due to an uncertain B field vector in the outer part of the detector. For instance, the effect could be the result of alignment uncertainties. However, we were led to this cut by the hypothesis that it is a magnetic field effect. And besides, it is not at all clear to us how to distinguish the magnetic field hypothesis from different explanations.

(b) "track-strip use fraction cut" – the track was excluded if a large fraction of planes used in fit had high multiplicity hits. Two examples of such tracks are shown in Fig.6. The systematic errors introduced into the fit parameter (q/p) for such tracks are shown in Fig.7. This figure shows N_{μ^+}/N_{μ^-}, for both the data and the Monte Carlo, as a function of the track-strip use fraction, where track-strip use fraction is defined as (# double ended strips in the track)/(total # strips in the event). There is a clear systematic bias in the way charge sign is determined for tracks with low strip-use fraction.

The track was excluded if track-strip use fraction < 0.35.

(c) the track was excluded if $(q/p)/\sigma_{q/p} < 2.0$, where (q/p) is the fit parameter returned by the Kalman filter and $\sigma_{q/p}$ is the error in the fit parameter. In Fig.8 we show N_{μ^+}/N_{μ^-}, the ratio of μ^+ to μ^-, as a function of $(q/p)/\sigma_{q/p}$. For $(q/p)/\sigma_{q/p} \geq 2.0$, the charge ratio is flat, suggesting that the charge sign and momentum are well fit. For $(q/p)/\sigma_{q/p} < 2.0$, as the ratio decreases monotonically toward 1, (q/p) becomes less realiably determined. For $(q/p)/\sigma_{q/p} = 1$, the charge sign is indeterminant and tracking information is clearly unreliable.

After cuts, there were 713,342 single-track events in the DF sample; 385,868 single-track events in the DR sample; and 237,894 single-track events in the MC sample.

Table 2. Effect of Analysis Cuts Applied to Cosmic Muon Data Samples

	Fraction Remaining		
cut	**DF**[†]	**DR**[†]	**MC**[†]
0. no cuts	1.0	1.0	1.0
1. 20 plane cut	0.759	0.758	0.763
2. 2m track length cut	0.755	0.754	0.758
3. fiducial cut	0.733	0.732	0.740
4. fit quality cuts			
(a) passed tracker internal consistency checks	0.733	0.730	0.739
(b) $\chi^2_{fitter}/ndf > 2.0$	0.692	0.692	0.721
(c) $\mathcal{A} \leq 0.89$	0.688	0.687	0.720
5. muon-like cut	0.687	0.687	0.720
6. timing quality cuts			
(a) double-ended strip cut	0.686	0.685	0.720
(b) $\chi^2_{dt/dy}/ndf > 3.0$	0.686	0.685	0.719
(c) directional consistency cut	0.686	0.685	0.719
7. charge-sign quality cuts			
(a) MIITIPOTDC	0.128	0.129	0.146
(b) track strip use fraction cut	0.126	0.127	0.145
(c) $(q/p)/\sigma_{q/p} < 2.0$	0.069	0.069	0.093

[†] DF = cosmic data set, forward field; DR = cosmic data set, reverse field; MC = Monte Carlo data set

There are two main differences in the cuts as applied to the data and as applied to the MC. Fewer MC events fail the χ^2_{fitter}/ndf cut because the MC events are in general cleaner than the data events. More important, the MC events are generated with the same magnetic field and alignment as is used in their reconstruction, whereas the data events are reconstructed with a field map that has systematic uncertainties in the outer regions of the detector and systematic uncertainties in the alignment.

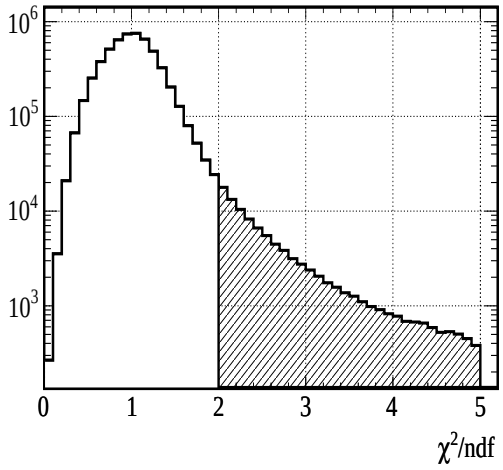

Figure 3. Distribution of χ^2/ndf for the SR fit to cosmic muon tracks. Shaded region shows cut at $\chi^2/ndf > 2.0$.

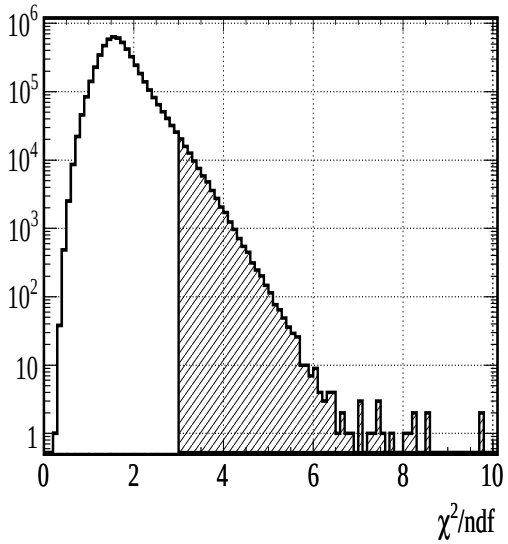

Figure 4. Distribution of $\chi^2_{dt/dy}/ndf$ for the time vs y-position fit for cosmic muon tracks. Shaded region shows cut at $\chi^2_{dt/dy}/ndf > 3.0$.

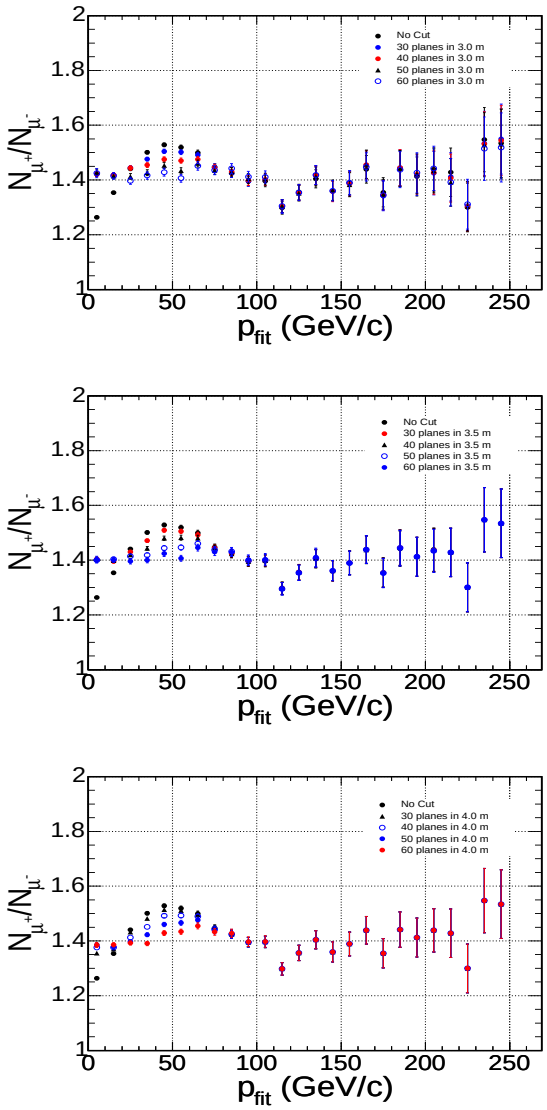

Figure 5. Muon charge ratio, N_{μ^+}/N_{μ^-} for the DR+DF data sets as a function of fit momentum for track fit information restricted to radii of (a) 3.0m, (b) 3.5m, and (c) 4.0m from the detector center. For each plot, the number of planes of information required has been varied from 0-60 planes. Cut chosen at 60 planes within 3.5m.

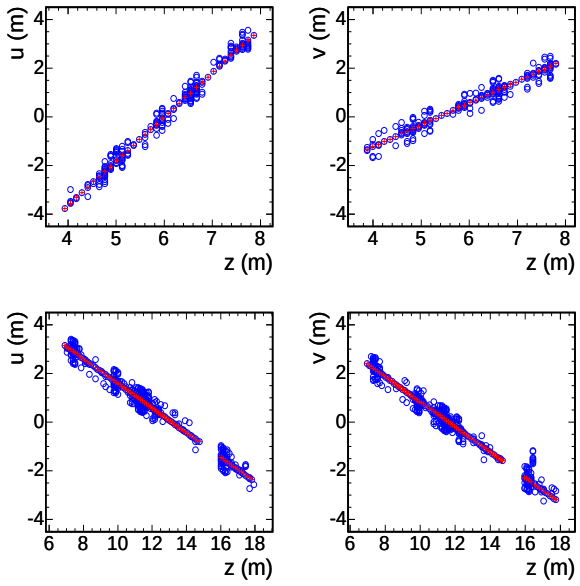

Figure 6. Examples of events with poor track strip use fraction.

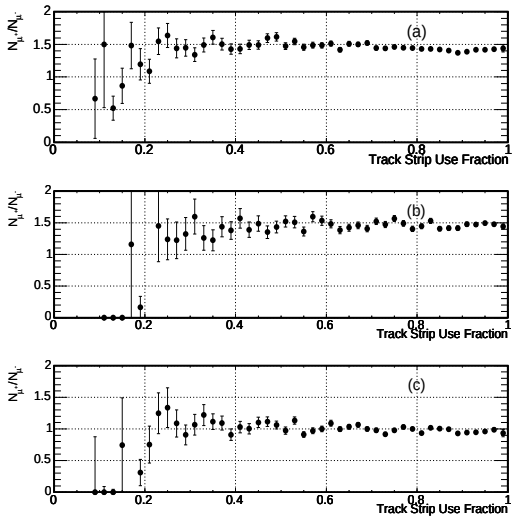

Figure 7. (a) The charge ratio of reconstructed muon tracks, N_{μ^+}/N_{μ^-} as a function of track strip use fraction for the DF data sample; (b) same plot for the MC sample; (c) the ratio of the data plot divided by the MC plot, (a) divided by (b). Cut chosen at track strip use fraction > 0.35.

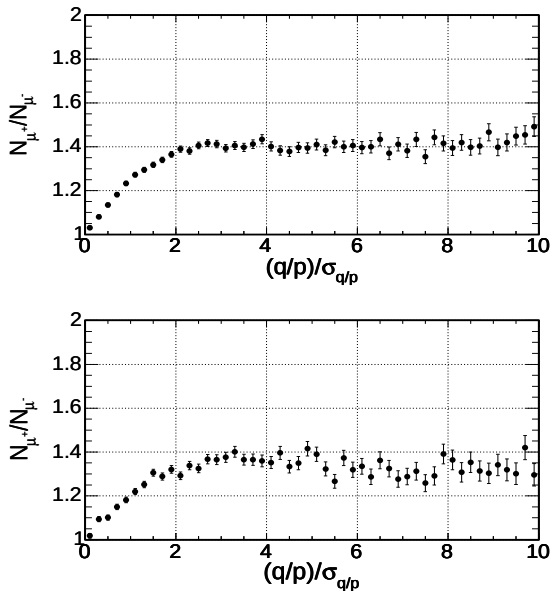

Figure 8. The N_{μ^+}/N_{μ^-} ratio for reconstructed muon tracks as a function of $(q/p)/\sigma_{q/p}$. (a) DF data distribution; (b) DR data distribution. Cut chosen at $(q/p)/\sigma_{q/p} > 2.0$ for both data sets.

A summary of the cuts applied to the data sets is given in Table 3.

Table 3. Summary of the Cuts Applied

	Fraction Remaining		
cut	**DF**†	**DR**†	**MC**†
No Cuts			
fraction remaining	1.0	1.0	1.0
number of events	14,705,956	7,735,811	2,812,704
Pre-Analysis/Run Cuts			
fraction remaining	0.703	0.722	0.913
number of events	10,338,287	5,592,290	237,894
Analysis Cuts			
fraction remaining	0.049	0.050	0.085
number of events	713,342	385,868	2,557,999

† DF = cosmic data set, forward field; DR = cosmic data set, reverse field; MC = Monte Carlo data set

We draw two main conclusions from our analysis procedure:

Conclusion 1: *Very hard cuts* are required to minimize systematic effects in charge sign identification for the cosmic muon data sample.

Conclusion 2: The Forward (DF) and Reverse (DR) data samples appear to have only very minor systematic differences between them after the cuts described above.

Conclusion 1 is a direct result of the fact that MINOS was not optimized as a cosmic ray detector. Most probably small systematic uncertainties in our understanding of the outer regions of the detector lead to large reconstruction errors in charge sign identification in the cosmic muons. As these detector uncertainties are resolved, we expect that the hard cuts required for proper charge sign identification can be softened.

The $1/\beta$ distribution for the events in the DF sample is shown in Fig.9. This distribution comes from fitting the slope to the the time of each hit as a function of the hit's distance from the track vertex. A Gaussian is superposed onto the data distribution. The mean is at 1.0, as expected, and the $\sigma = 0.026$ suggests timing errors of 2.6%. The tails of the $1/\beta$ distribution are wider than the Gaussian distribution predicts which suggests that systematic timing errors are present in tracks with β significantly different from 1.

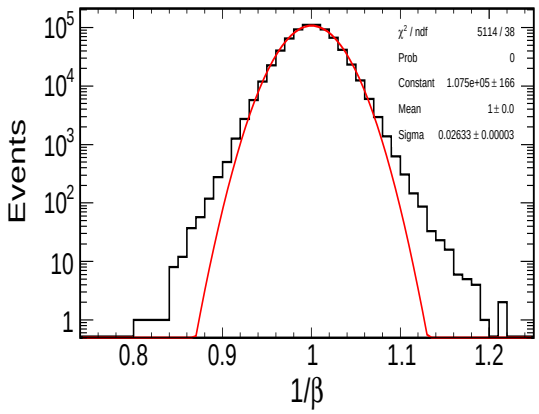

Figure 9. The $1/\beta$ distribution for the muons in the DF data set

3 Cosmic Muon Distributions

We used the data sets described above to construct several distributions of single track cosmic muon events. The first histograms we investigated were ones

without charge sign reconstruction in order to make comparisons with the Monte Carlo distributions constructed using the results of the Soudan 2 collaboration [1]. We then proceeded to investigate underground cosmic muon distributions with charge sign reconstruction, which for MINOS fall in a previously unexplored regime of muon surface energy, $E_{surf} > 400$ GeV.

3.1 Distributions without Charge Separation

3.1.1 Distributions as a function of Horizon Coordinates

First we used our data sets to construct muon distributions in the horizon coordinates zenith angle θ and azimuthal angle ϕ. We then superposed onto them the Standard MINOS atmospheric muon Monte Carlo based on the Soudan 2 rock distributions [1]. The MC distributions have been normalized to equal area for comparison. Some explanation is useful for the coordinates used in Figs. 10 and 11. Horizon coordinates are defined in a spherical, polar coordinate frame, but not in the standard way. The polar or zenith angle θ is measured from the zenith, $\theta = 0°$ to the horizon $\theta = 90°$, as expected. The azimuthal angle ϕ, however, is defined with $\phi = 0$ due North, but increasing in a left-handed sense to the East ($\phi = 90°$), South ($\phi = 180°$), and West ($\phi = 270°$). In our analyses, the sky is divided into equal solid angle bins, $\Delta\Omega = \Delta\cos\theta \times \Delta\phi$, with the binnings in Figs. 10 and 11 being $\Delta\cos\theta = 0.02$ and $\Delta\phi = 6°$, respectively. In addition, the azimuthal angle in Fig. 11 from $\phi = 0° - 60°$ has been offset by 360° to show a continuous distribution from the North.

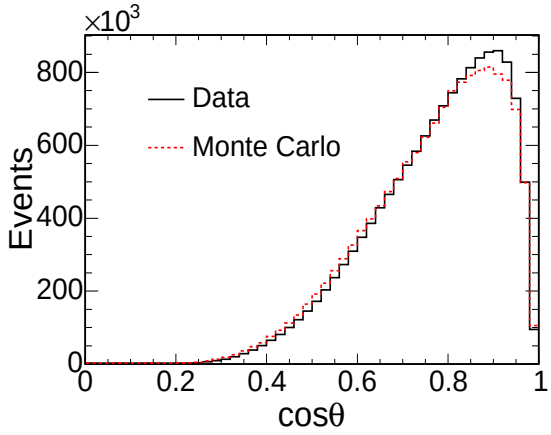

Figure 10. The $\cos\theta$ distribution for the DF+DR data sets (solid line), without charge separation, compared with the MC data set (dashed line). The distributions have been normalized to have equal area.

The dip at the zenith, $\cos\theta = 1$ is easily understood as a solid angle effect. Assuming that cosmic rays arrive essentially uniformly in solid angle, there

will be a dip at the zenith where the $\sin\theta \rightarrow 0$ factor in solid angle drives $\Delta\Omega = \sin\theta\Delta\theta\Delta\phi \rightarrow 0$. The falloff from the peak is mostly due to increasing rock depth, which requires higher energy muons to reach the detector from the surface, and the power law falloff of cosmic ray flux at the surface.

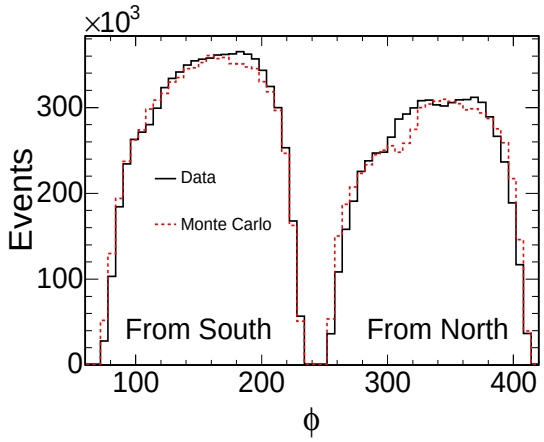

Figure 11. The azimuthal angle distribution for the DF+DR data sets (solid line) compared with MC data set (dashed line). The distributions have been normalized to have equal area. The azimuthal angle distribution from $\phi = 0^\circ - 60^\circ$ has been offset by 360° to show a continuous distribution from the North.

The structure of azimuthal angle distribution can be understood as a combination of detector characteristics and rock map effects. The two dips are a result of the detector's parallel plane constuction. The 20 plane cut eliminates events from detector azimuths $\phi_{det} = 90^\circ, 270^\circ$. But the detector points back to Chicago so azimuth is offset $\approx 26.5^\circ$ from due north, which accounts for the offset in the cosmic ray minima in Fig.11. The difference in relative heights of the peaks is due entirely to differences in rock depth and rock density.

As these figures make clear, the MC does not describe the data particularly accurately. In the $\cos\theta$ distributions, there are deviations at low zenith angles. There are also deviations in the azimuthal angle distribution, particularly from the North. It is likely that these deviations result at least in part from uncertainties in the rock map.

3.1.2 Distributions as a function of Celestial Coordinates

Source searches are typically carried out in the celestial coordinates declination, δ, and right ascension, α. In Figs.12 and 13 we show the distributions of cosmic muons in these coordinates. Since the same declinations are continuously visible from the same location, the declination distribution will be independent of live-time. On the other hand, the right ascensions visible to the detector

vary uniformly with a period equal to a sidereal day. So the right ascension distribution shows the effects of live time.

Fig.12a shows the $\cos\delta$ distribution used in making an equal solid angle sky map. The features of this distribution are more easily understood with the δ distribution shown in Fig.12b. As described above, there is a dip in the muon distribution at the zenith, which for Soudan is $\delta \approx 48°$. The falloff at high declinations is due to the fact that there are 11.5° in the 0.98-1.0 bin in $\cos\delta$ but only 1.3° in the 0.50-0.52 bin. The falloff at low declinations is again due to rock depth and the falling cosmic muon energy spectrum.

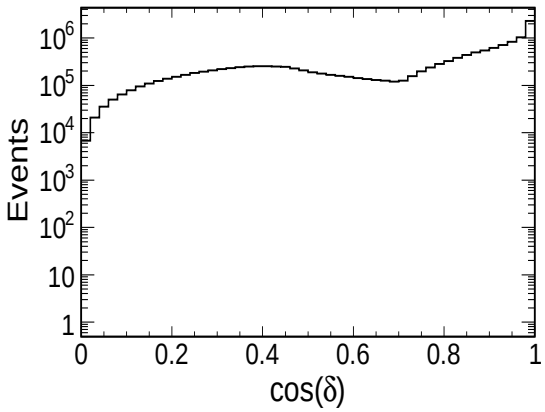

Figure 12a. The $\cos\delta$ distribution for the DF+DR data sets

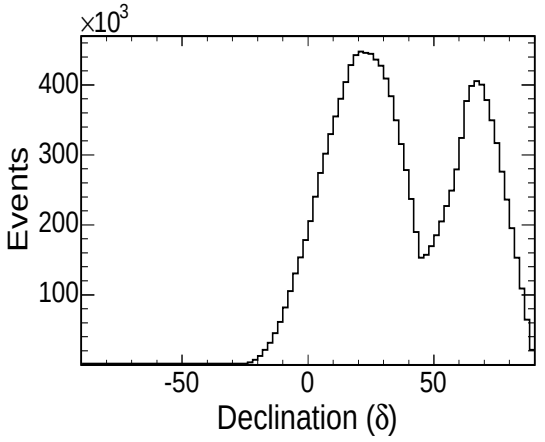

Figure 12b. The δ distribution for the DF+DR data sets

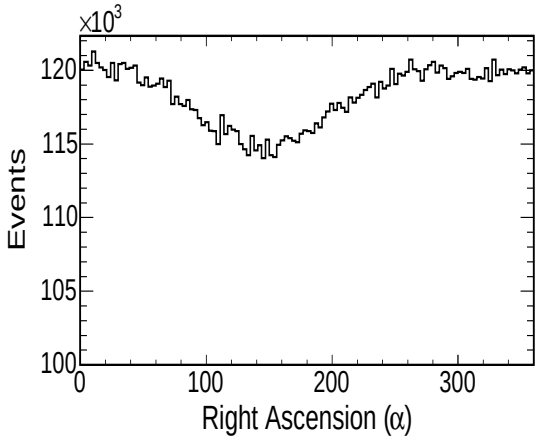

Figure 13. The right ascension α distribution for the DF+DR data sets

3.2 Distributions with Charge Separation

An important motivation for this work the was demonstration that we understand charge sign determination in MINOS. For that purpose, we have first generated charge sign separated distributions from the DF + DR data sets to compare with the total data sets to see if there were any gross peculiarities. In Fig. 14 we show the reconstructed momentum spectra for the DF+DR data sets; in Fig. 15 we show the slant depth distributions; in Fig. 16 we show the distributions as a function of $\cos\theta$; and in Fig. 17 we show the distributions as a function of azimuth ϕ. The charge sign distributions all look consistent with the total data sets.

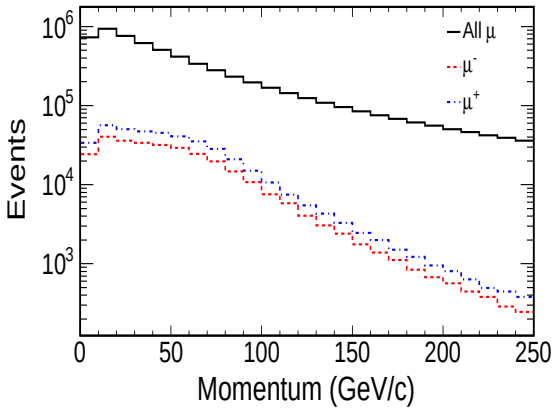

Figure 14. The reconstructed momentum spectra for the DF+DR data sets: (a) total spectrum; (b) μ^+ spectrum; (c) μ^- spectrum

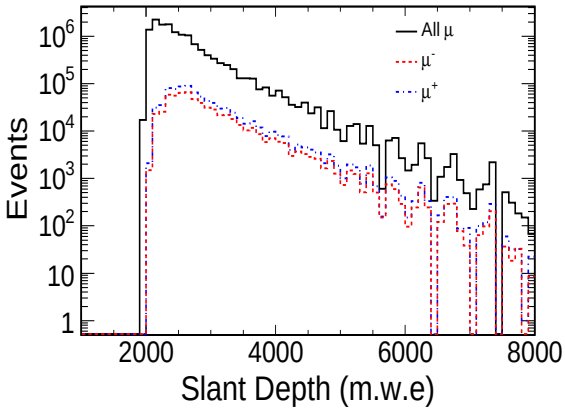

Figure 15. The slant depth distributions for the DF+DR data sets: (a) total data set; (b) μ^+ distribution; (c) μ^- distribution

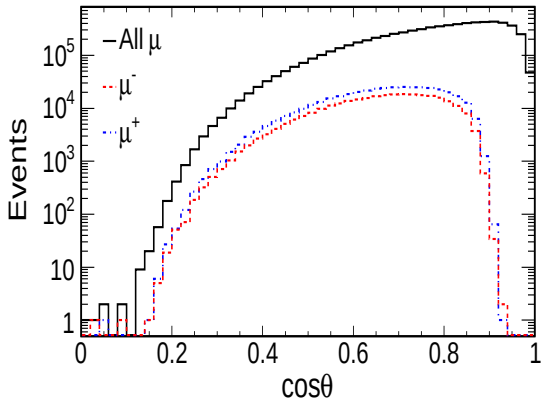

Figure 16. The $\cos\theta$ zenith angle distributions for the DF+DR data sets: (a) total data set; (b) μ^+ distribution; (c) μ^- distribution

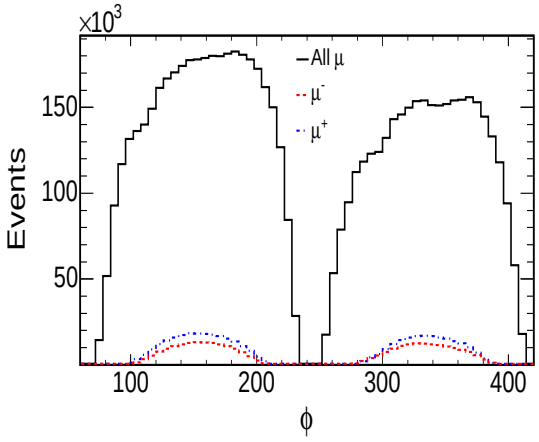

Figure 17. The azimuthal angle ϕ distributions for the DF+DR data sets: (a) total data set; (b) μ^+ distribution; (c) μ^- distribution

3.2.1 Charge Ratio Distributions

One of the prime motivations for this investigation was to determine the N_{μ^+}/N_{μ^-} ratio at the depth of MINOS. With its magnetic field, MINOS is the first deep detector that can make this measurement. Below we present several distributions of the charge ratio N_{μ^+}/N_{μ^-} and compare these with Monte Carlo expectations.

An important concept in many of these distributions is the notion of focusing. MINOS was built primarily to study μ^- coming from Fermilab and the toroidal MINOS magnetic field was therefore designed to bend μ^- coming from the South toward the center of the detector. Conversely, μ^+ coming from the South are bent out of the detector. When the magnetic field is reversed, the opposite occurs – μ^+ coming from the South are bent toward the center of the detector and μ^- coming from the South are bent out of the detector. (A detailed discussion of focusing can be found in Brian Rebel's dissertation [3].) Consequently, when data from Forward and Reverse field running are added, weighted by live-time, the effects of focusing should cancel. In addition, any other systematic effects that depend on the direction of the magnetic field should also cancel when Forward and Rerverse field data are added.

Figs. 18a and 18b show the muon charge ratio, N_{μ^+}/N_{μ^-}, as a function of zenith angle. In the top panel of these figures, the data are shown. In the middle panel, the MC prediction for this distribution is shown. In the bottom panel, the ratio of data to the MC distributions is shown. The data in Figs. 18a and 18b do not reach the zenith because of the requirement that there be 60 planes of information on a track within 3.5 meters or the detector center. The turn-up at low zenith angles for the DF data set and the turn-down for the DR data set are clear examples of focusing and are seen in the MC. For the live-time weighted average of the data, Fig. 19, there is a significant cancellation of

systematics except at high zenith angle. This upturn could be the effect of low statistics or a real rise in the charge ratio at large depths.

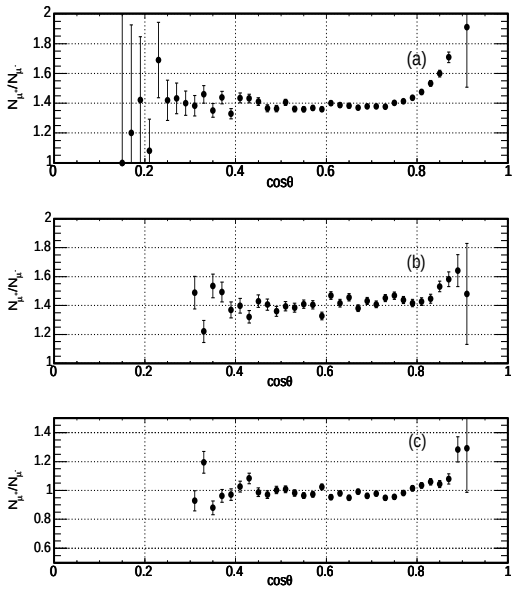

Figure 18a. (a) The charge ratio N_{μ^+}/N_{μ^-} vs. $\cos\theta$ for the DF data set; (b) the MC prediction for this ratio; (c) the ratio of histogram (a)/histogram (b)

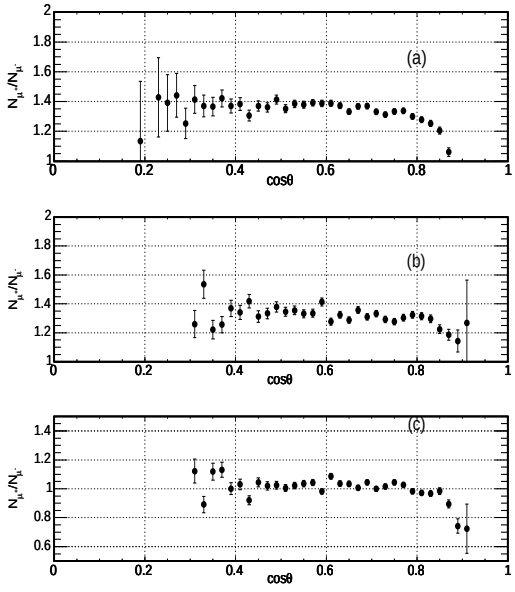

Figure 18b. (a) The charge ratio N_{μ^+}/N_{μ^-} vs. $\cos\theta$ for the DR data set; (b) the MC prediction for this ratio; (c) the ratio of histogram (a)/histogram (b)

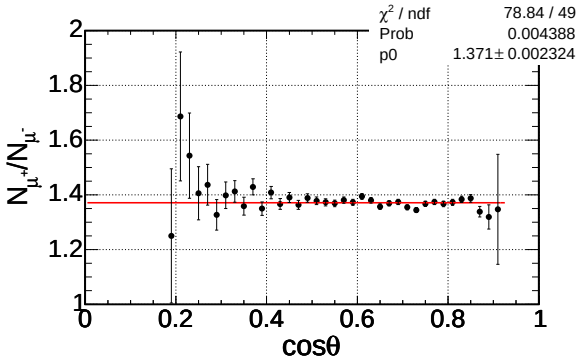

Figure 19. The live-time weighted average of the DF and DR distributions given in Fig.18a(a) and Fig.18b(a). This distribution represents the charge ratio vs. $\cos\theta$ with corrections for systematic uncertainties in the magnetic field and detector alignment. A fit to a constant ratio gives $N_{\mu^+}/N_{\mu^-} = 1.37$

Figs. 20a and 20b show the charge ratio N_{μ^+}/N_{μ^-} as a function of azimuthal angle ϕ. The azimuthal angle distribution from $\phi = 0° - 60°$ has been offset by 360° to show a continuous distribution from the North. The 20 plane cut eliminates events from azimuths $\phi_{det} = 63.5°$, 243.5°. The upturn and downturn at these minima are due to focusing effects [3]. The MC does not reproduce the distributions with great precision, probably because of the unknown composition of the Soudan rock (K. Ruddick). In the live-time weighted distribution in Fig. 21, the systematics cancel.

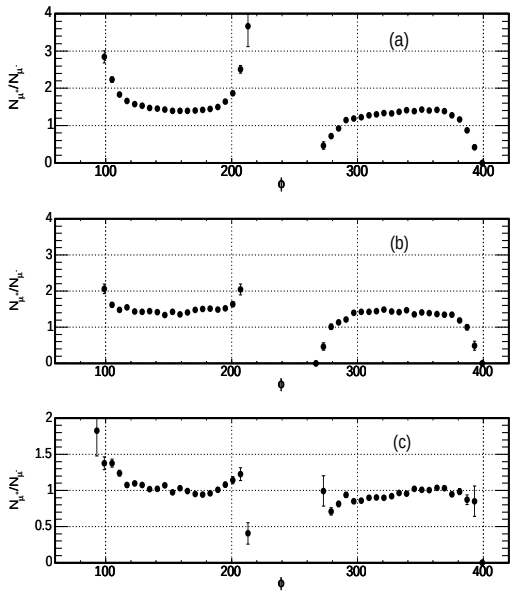

Figure 20a. (a) The charge ratio N_{μ^+}/N_{μ^-} vs. azimuthal angle ϕ for the DF data set; (b) the MC prediction for this ratio; (c) the ratio of histogram (a)/histogram (b)

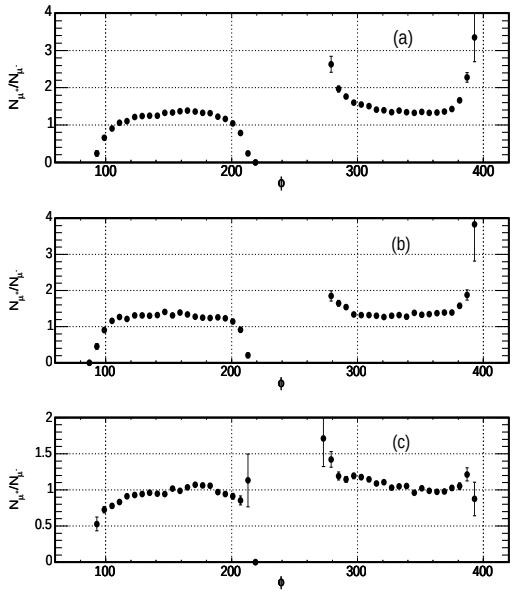

Figure 20b. (a) The charge ratio N_{μ^+}/N_{μ^-} vs. azimuthal angle ϕ for the DR data set; (b) the MC prediction for this ratio; (c) the ratio of histogram (a)/histogram (b)

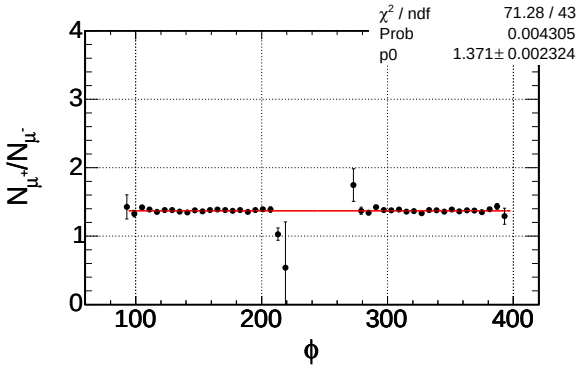

Figure 21. The live-time weighted average of the DF and DR distributions given in Fig.20a(a) and Fig.20b(a). This distribution represents the charge ratio vs. azimuthal angle θ corrected for systematic uncertainties in the magnetic field and detector alignment. A fit to a constant ratio gives $N_{\mu^+}/N_{\mu^-} = 1.37$

Figs. 22a and 22b show the charge ratio N_{μ^+}/N_{μ^-} as a function of fit momentum, $\mathbf{p}_{fit}$. Although there are no obvious focusing effects associated with these distributions, there are clear systematics in the distributions that reverse when the field is reversed. In our search to improve charge sign quality, we optimized our cuts against these distributions to minimize systematics. The live-time weighted average, shown in Fig. 23, is nearly free of systematics below 100 GeV/c.

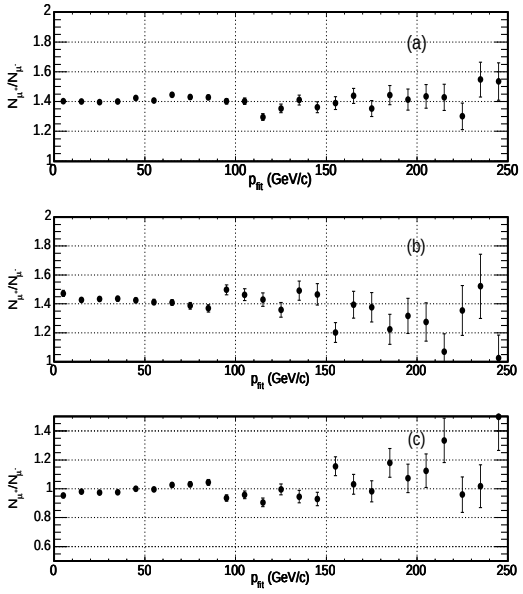

Figure 22a. a) The charge ratio N_{μ^+}/N_{μ^-} vs. fit momentum $\mathbf{p}_{fit}$ (GeV/c) for the DF data set; (b) the MC prediction for this ratio; (c) the ratio of histogram (a)/histogram (b)

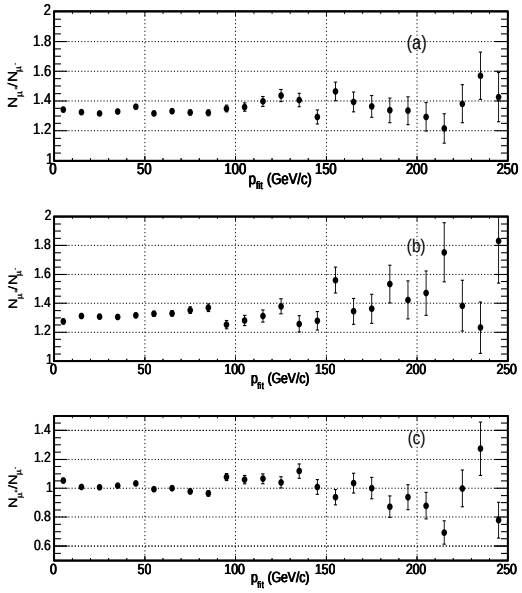

Figure 22b. a) The charge ratio N_{μ^+}/N_{μ^-} vs. fit momentum $\mathbf{p}_{fit}$ (GeV/c) for the DR data set; (b) the MC prediction for this ratio; (c) the ratio of histogram (a)/histogram (b)

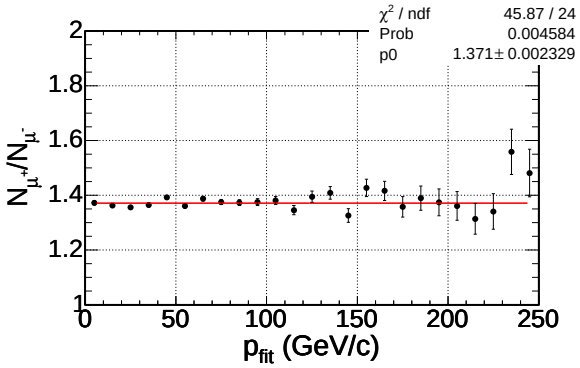

Figure 23. The live-time weighted average of the DF and DR distributions given in Fig.22a(a) and Fig.22b(a). This distribution represents the charge ratio vs vs. fit momentum $\mathbf{p}_{fit}$ (GeV/c) corrected for systematic uncertainties in the magnetic field and detector alignment. A fit to a constant ratio gives $N_{\mu^+}/N_{\mu^-} = 1.37$

Figs. 24a and 24b show the charge ratio N_{μ^+}/N_{μ^-} as a function of slant depth. Since low zenith angles imply shallow slant depths and high zenith angles imply large slant depths, these distributions are closely related to the zenith angle distributions in Figs. 18a and 18b. The live-time weighted average is shown in Fig. 25. As the other live-time average distributions, the residual systematics that have not been removed by the charge sign cuts are minimized.

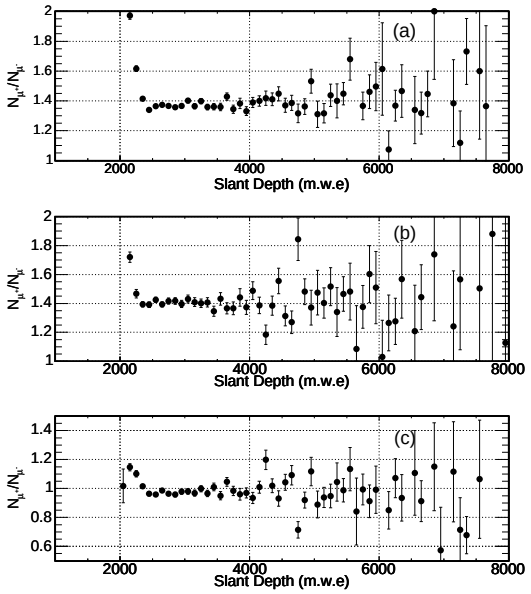

Figure 24a. (a) The charge ratio N_{μ^+}/N_{μ^-} vs. slant depth [1] for the DF data set; (b) the MC prediction for this ratio; (c) the ratio of histogram (a)/histogram (b)

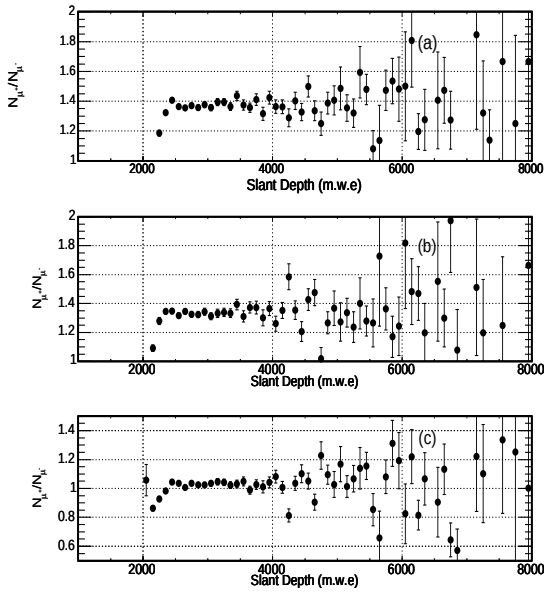

Figure 24b. (a) The charge ratio N_{μ^+}/N_{μ^-} vs. slant depth [1] for the DR data set; (b) the MC prediction for this ratio; (c) the ratio of histogram (a)/histogram (b)

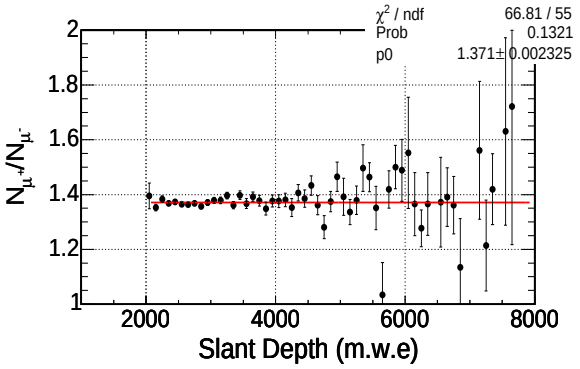

Figure 25. The live-time weighted average of the DF and DR distributions given in Fig.24a(a) and Fig.24b(a). This distribution represents the charge ratio vs vs. slant depth corrected for systematic uncertainties in the magnetic field and detector alignment. A fit to a constant ratio gives $N_{\mu^+}/N_{\mu^-} = 1.37$

Figs. 26a and 26b show the charge ratio N_{μ^+}/N_{μ^-} as a beam azimuth. These distributions are ones used extensively by the Argonne group in their analyses. There is a clear systematic wave in the charge ratio when plotted in these coordinates that seems to be seen in the MC. The live-time weighted average is

shown in Fig. 25. Although the source of the systematic wave seen in the data when plotted in these coordinates is not apparent, the cuts that remove the systematics when the charge ratio is plotted against other variables also remove the systematics when plotted again beam azimuth.

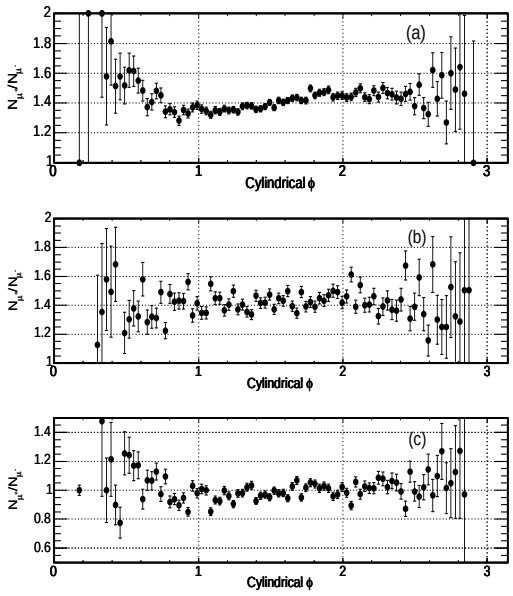

Figure 26a. (a) The charge ratio N_{μ^+}/N_{μ^-} vs. beam azimuth for the DF data set; (b) the MC prediction for this ratio; (c) the ratio of histogram (a)/histogram (b)

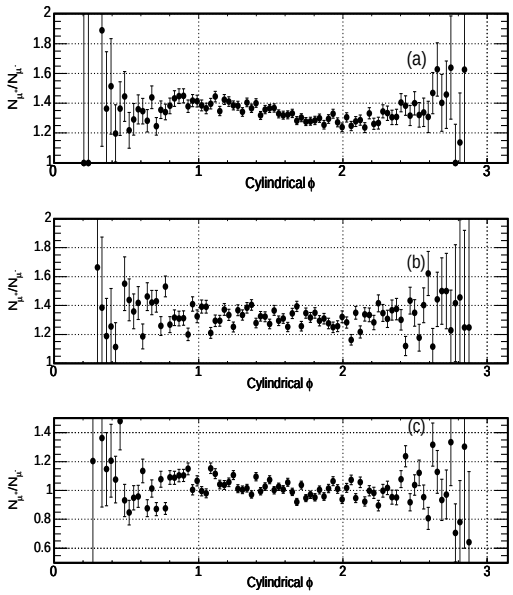

Figure 26b. (a) The charge ratio N_{μ^+}/N_{μ^-} vs. beam azimuth for the DR data set; (b) the MC prediction for this ratio; (c) the ratio of histogram (a)/histogram (b)

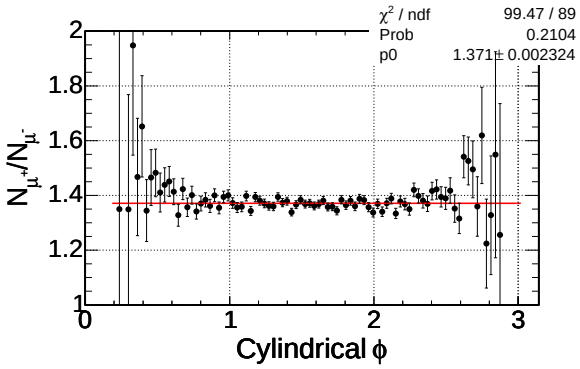

Figure 27. The live-time weighted average of the DF and DR distributions given in Fig.26a(a) and Fig.26b(a). This distribution represents the charge ratio vs vs. beam azimuth corrected for systematic uncertainties in the magnetic field and detector alignment. A fit to a constant ratio gives $N_{\mu^+}/N_{\mu^-} = 1.37$

3.2.2 The N_{μ^+}/N_{μ^-} Ratio at the MINOS Far Detector

The live-time weighted averages of the charge ratio N_{μ^+}/N_{μ^-} when plotted against several different variables (Figs. 19, 21, 23, 25, 27) all give similar results. When fit with a constant charge ratio fitting function, the result is that

$N_{\mu^+}/N_{\mu^-} = 1.371 \pm .1 \pm 0.002$ with $\chi^2/ndf \sim 1.2 - 1.8$. This consistency suggests that the same systematics affect the data and they are independent of how the data are plotted. In fact, it was our intention to rid the data sets of peculiar systematics that affect, say, the $\cos\theta$ distribution or the beam azimuth distribution.

Although our data strongly support the result that $N_{\mu^+}/N_{\mu^-} = 1.37$, we believe the error on the charge ratio given by the fitting procedure is an underestimate. Another method to estimate the error (suggested by Stan, or at least we think suggested by Stan) is to make a linear fit to the data and use the slope from the fit to estimate the variation of the charge ratio over the range of the fit. We have chosen to use this approach with the charge ratio as a function of fit momentum, Fig. 25. We use this distribution because it seems to be the one least succeptible to focusing effects and rock map uncertainties. The coordinate distributions, those that plot the charge ratio vs $\cos\theta$, azimuth ϕ, or beam azimuth, are clearly affected by focusing. The charge ratio vs. rock depth distribution is affected by focusing at the shallowest depths ($\cos\theta$) and by rock map uncertainties at the largest depths. In Fig. 28 we show a straight line fit to the charge ratio as a function of fit momentum. Although the χ^2/ndf for this fit and the fit to a constant charge ratio are essentially equivalent, we prefer the constant charge ratio fit because it is simpler (Occam's Razor).

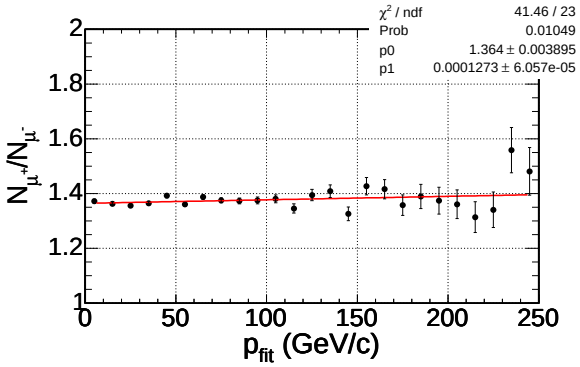

Figure 28. The live-time weighted average of the DF and DR distributions given in Fig.22a(a) and Fig.22b(a). A straight line fit gives $N_{\mu^+}/N_{\mu^-} = 1.37$

Our estimate of the error on the charge ratio is $0.0001273 \times 250 = 0.032$. Our result for the charge ratio is, therefore,

$$N_{\mu^+}/N_{\mu^-} = 1.37 \pm 0.03. \quad (1)$$

4 Results

4.1 Vertical Muon Intensity at the MINOS Far Detector

The vertical muon intensity $I(h)$ at slant depth h at the MINOS far detector is given by [4]

$$I(h) = \frac{1}{\Delta T} \frac{\sum_i (m_i N_i)}{\sum_j (\Delta\Omega_j A_j \epsilon_j / \cos\theta_j)}, \tag{2}$$

where ΔT is the live-time, $\sum_i (m_i N_i)$ is the number of muons N of multiplicity m at slant depth h, $\Delta\Omega$ is the bin solid angle, and $A_j(\cos\theta, \phi)$, $\epsilon_j(\cos\theta, \phi)$ are the projected area of the detector and the efficiency of the detector as a function of the zenith angle and azimuth, repectively.

The projected area of the MINOS far detector in direction ($\cos\theta$, ϕ), $A_j(\cos\theta_j, \phi_j)$, was computed by first defining the unit vector along this direction, $\hat{\mathbf{n}}_\mu = \hat{\mathbf{n}}_\mu(\cos\theta, \phi)$ and then defining the normal for each of the eight surfaces of the MINOS far detector, $\hat{\mathbf{n}}_\mathbf{i}$, where $i = 1 - 8$. The projected area is then given by

$$A_j(\cos\theta_j, \phi_j) = \sum_{i=1}^{8} (-\hat{\mathbf{n}}_\mathbf{j} \cdot \hat{\mathbf{n}}_\mathbf{i}) S_i, \tag{3}$$

for all $(-\hat{\mathbf{n}}_\mu \cdot \hat{\mathbf{n}}_\mathbf{i}) \geq 0$ and where S_i is the area of the ith surface of the MINOS detector. The projected area in solid angle bins $\Delta\cos\theta \times \Delta\phi = 0.02 \times 6^\circ$ is shown in Fig.29.

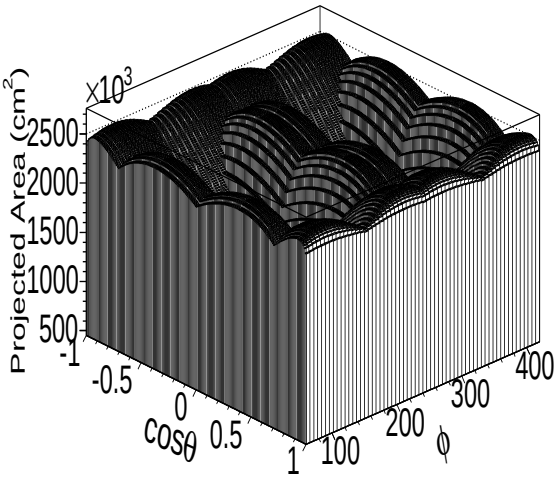

Figure 29. Projected area of the far MINOS detector as a function of horizon coordinates

The efficiency of the far detector, $\epsilon_j(\cos\theta, \phi)$, for the reconstruction of single muon tracks was computed with Monte Carlo events from the relation

$$\epsilon_j(\cos\theta_j, \phi_j) = \sum_i \left[N_i(\cos\theta_j, \phi_j)\right]_{cuts} / \sum_i \left[N_i(\cos\theta_j, \phi_j)\right]_{no\ cuts}, \qquad (4)$$

where $\left[N_i(\cos\theta_j, \phi_j)\right]_{cuts}$ is the number of muons from direction $(\cos\theta_j, \phi_j)$ with cuts applied; $\left[N_i(\cos\theta_j, \phi_j)\right]_{no\ cuts}$ is the same quantity without cuts. The efficiency in solid angle bins $\Delta\cos\theta \times \Delta\phi = 0.02 \times 6^\circ$ is shown in Fig.30.

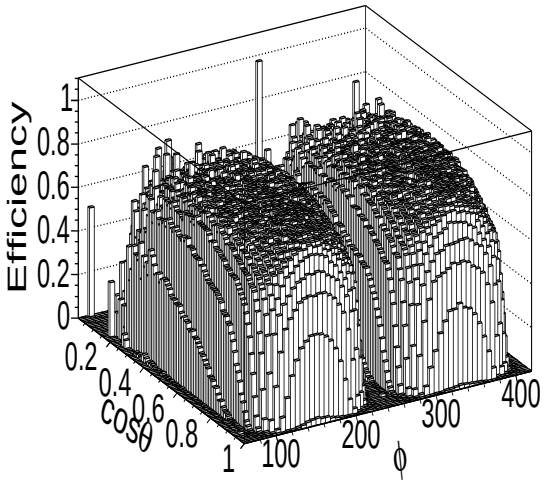

Figure 30. Efficiency of the MINOS far detector to single atmospheric muons

The acceptance of the MINOS far detector for single cosmic ray muons, $(A\Omega) = \sum_i (\Delta\Omega_j A_j \epsilon_j)$, is shown in Fig. 31.

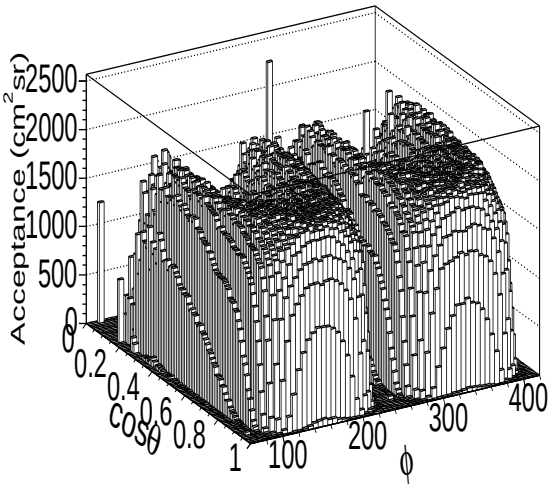

Figure 31. Acceptance of the MINOS far detector to single atmospheric muons

The total acceptance for the MINOS far detector to single atmospheric muons is 7.62×10^2 m^2 sr. Using eq.(2), we have computed the vertical intensity for single muons in the MINOS hall. To compare our results with those of other detectors at the depth of the MINOS far detector [5], we must correct our single muon data for multiple muon events. To make this correction we use the factor 1.04, which was based on the multiplicity data given in Table 4. These multiplicity data were compiled by Mark Thomson from a day of MINOS far data using his event classification algorithm and has an assumed error of ∼5-10%. Our correction factor assumes that multiplicity is independent of depth in our data sample. In Fig. 32 we show the vertical intensity of muons in the MINOS far detector hall.

Table 4. Event Multiplicity in MINOS

Event Multiplicity	Number of Events	Fraction of Total
1 muon	40,875	0.96
2 muons	1,282	0.030
3 muons	226	0.0053
4 muons	86	0.0020
5 muons	26	0.00061
6 muons	17	0.00040
7 muons	12	0.00028
8 muons	1	0.000023
9 muons	1	0.000023

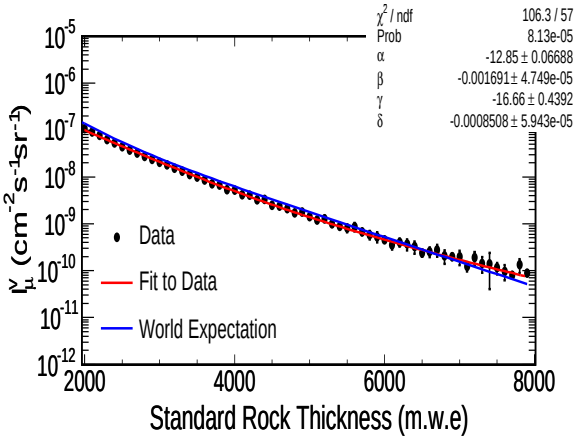

Figure 32. Vertical intensity of muons in the MINOS far detector hall from eq.(2). The single muon data was corrected for multiples using Table 4. Superposed onto this distribution is the fit function of Crouch [6], labeled 'World Expectation', and a fit to the form of eq.(5) labeled 'Fit to Data'.

To compare the MINOS vertical intensity corrected for multiples shown in Fig. 32 with the fit to the measurements of other experiments, we have superposed the fit function of Crouch [6], $I_f(h)$,

$$I_f(h) = \exp(\alpha + \beta h) + \exp(\gamma + \delta h), \tag{5}$$

onto the data, where the depth h is in m.w.e., and $\alpha = -11.22 \pm 0.17$, $\beta = (-0.00262 \pm 0.00013)\, m.w.e.^{-1}$, $\gamma = -14.10 \pm 0.14$, and $\delta = (-0.001213 \pm 0.000021)\, m.w.e.^{-1}$. This fit is labeled 'World Expectation' in Fig. 32. The $\chi^2/ndf = 1282/57$ for this fit is quite poor. A fit to the MINOS data using the form of eq.(5) yields significantly different parameters, $\alpha = -12.85 \pm 0.067$, $\beta = (-0.00169 \pm 0.000047)\, m.w.e.^{-1}$, $\gamma = -16.66 \pm 0.044$, and $\delta = (-0.00851 \pm 0.000059)\, m.w.e.^{-1}$, and a significantly improved $\chi^2/ndf = 106.3/57$. This fit is labeled 'Fit to Data' in Fig. 32.

We used the charge separated data and efficiencies for μ^+ and μ^- computed according to eq.(4) in eq.2) to determine the vertical intensity for the charge separated species. These intensities are shown in Fig. 33. We find that the vertical intensities for the charge separated species are quite similar in form, as would be expected. To test whether the charge species follow the same relation as the fit to the total data, we fit the μ^+ data to the form of eq.(5). This fit yields the parameters, $\alpha = -12.52 \pm 0.039$, $\beta = (-0.00185 \pm 0.0003)\, m.w.e.^{-1}$, $\gamma = -15.78 \pm 0.16$, and $\delta = (-0.000942 \pm 0.000025)\, m.w.e.^{-1}$, and $\chi^2/ndf = 174.4/57$. This fit is marginally consistent with the fit to the total data set and is shown superposed onto the μ^+ data in Fig. 34.

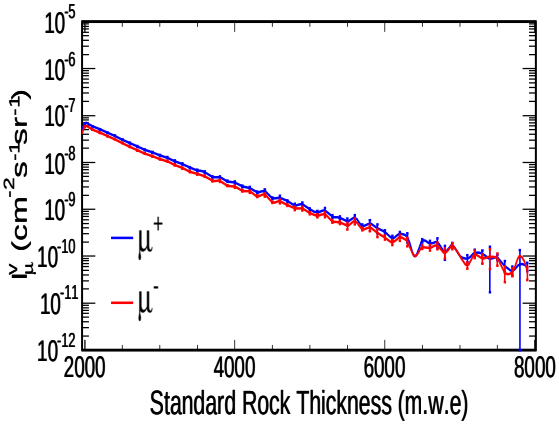

Figure 33. Vertical intensity of μ^+ and μ^- in the MINOS far detector hall from eq.(2).

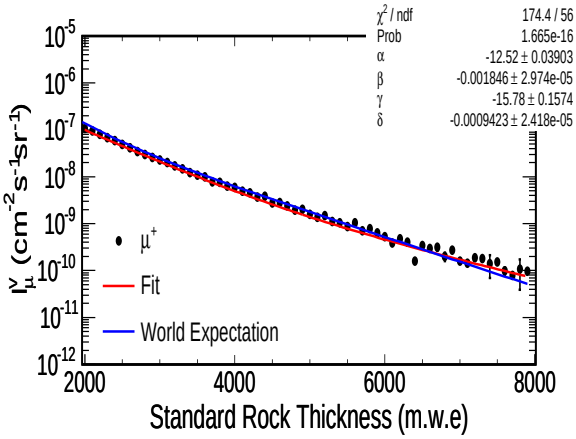

Figure 34. Vertical intensity of μ^+ with the fit function of Crouch, eq.(5), superposed.

4.2 Seasonal Variations

4.2.1 Correlations of Intensity Variations with Atmospheric Temperature

Underground muons originate primarily from the decay of mesons produced in high energy interactions between primary cosmic ray particles and atmospheric nuclei [2]. As has been discussed elsewhere [7], fluctuations in atmospheric temperature lead to variations in the muon intensity observed underground.

The dependence of muon intensity variations on the atmospheric temperature is often expressed phenomenologically as [8]:

$$\frac{\Delta I_\mu}{I_\mu^0} = \int_0^\infty dX\, \alpha(X)\, \frac{\Delta T(X)}{T(X)}. \tag{6}$$

In this equation, $I_\mu^0 = I_\mu(T_0, > E_{th})$ is the differential muon intensity integrated from the threshold energy required for muons at the surface to reach and be detected by MINOS, $E_{th}(\approx 400$ MeV), to infinity, assuming the atmosphere is isothermal at temperature T_0, and ΔI_μ are fluctuations about I_μ; $\alpha(X)$ is the "temperature coefficient" that relates fluctuations in the atmospheric temperature at depth X, $\Delta T(X)/T(X)$, to the fluctuations in the integral muon intensity; and the integral extends over atmospheric depth from the altitude of muon production, typically at $\sim$ 20 km, to the ground. The temperature coefficient for a deep detector like MINOS is dominated by a positive correlation between the underground muon intensity and the atmospheric temperature. As the atmospheric temperature increases, the density of the air decreases and fractionally more pions/kaons decay to muons before interacting.

In this analysis, the goal is the experimental determination of α which can then be related to the physics of cosmic ray muon production. To put eq.(6) in a form suitable for the experimental determination of α, we write the integral muon intensity

$$I_\mu = \frac{N_i/t_i}{\epsilon A_{eff}\Omega},$$

where N_i are the single muons observed during live time t_i, ϵ is the efficiency for the reconstruction of single muon tracks, A_{eff} is the detector effective area, and Ω is the total solid angle viewed by the detector. For data-taking over periods of weeks to months, A_{eff} and Ω are constant. The fluctuations in the integral muon intensity are then

$$\begin{aligned} \Delta I_\mu/I_\mu &= \left[\frac{\Delta N_i/t_i}{\epsilon A_{eff}\Omega}\right] \Big/ \left[\frac{N_i/t_i}{\epsilon A_{eff}\Omega}\right] = \left[\Delta N_i/t_i\right] \Big/ \left[N_i/t_i\right] \\ &= \Delta R_\mu/R_\mu \approx (R_\mu - \bar{R}_\mu)/\bar{R}_\mu, \end{aligned} \tag{7}$$

where $R_\mu = N_i/t_i$ is the muon rate observed underground during live time t_i and $\bar{R}_\mu = \sum N_i / \sum t_i$ is the average muon rate over the total data-taking period $\sum t_i$.

By introducing the so-called "effective temperature", T_{eff} [8], the integral in eq.(6) becomes

$$\begin{aligned} \int_0^\infty dX \alpha(X)\, \frac{\Delta T(X)}{T(X)} &= \alpha_T\, \frac{\Delta T_{eff}}{T_{eff}} \\ &\approx \alpha_T (T_{eff} - \bar{T}_{eff})/\bar{T}_{eff}, \end{aligned} \tag{8}$$

where α_T is the atmospheric depth-weighted temperature coefficient and $\bar{T}_{eff}$ is the average effective temperature during the data-taking period, $\sum t_i$. With these approximations, eq.(6) can be written

$$\Delta R_\mu / \bar{R}_\mu = \alpha_T \, \Delta T_{eff} / \bar{T}_{eff}, \tag{9}$$

where $\Delta T_{eff} = T_{eff} - \bar{T}_{eff}$.

The aim of this analysis is to compare the measured value of α_T with its expected value [7]

$$< \alpha_T >_\pi = (T/N_\mu)(\partial N_\mu / \partial T) = \left\langle \, 1 \Big/ \left[1 + \frac{\gamma}{(\gamma+1)} \times \frac{\epsilon_\pi}{1.1 \, E_{th} \cos\theta} \right] \right\rangle, \tag{10}$$

where $E_{th} \cos\theta$ is the product of the threshold energy, E_{th} and $\cos\theta$, for events in the muon sample, and γ is the spectral index of the muon intensity.

4.2.2 Measurements of Seasonal Variations

Currently we do not have the atmospheric temperature measurements required to compute the correlation coefficient α_T. However, we can search for the seasonal variations as a test of our understanding of our muon data sample. In Figs. 35 and 36, we show the seasonal variations in the DF and DR data sets, respectively. In these figures, the statistic $(R_\mu - \bar{R}_\mu)/\bar{R}_\mu$ is plotted for two month intervals, where $\bar{R}_\mu$ is the average over the whole data set. In the upper left panels, the total data set without charge separation cuts is shown. In the lower left and lower right panels, the charge separated data sets are shown. Overall these distributions agree with the expectation that the rates increase in the summer and decrease in the winter. In both the total data sets and the charge separated data sets, the peak-to-peak variations are of order 3-4%. For the DF data set, however, there is an unexpected dip in months 3-4 that is not seen in the charge separated data sets. For the charge ratio, in the upper right panels, there is no evidence for seasonal variations as shown by the χ^2/ndf of 2.3/5 and 1.1/4 for the DF and DR data sets, respectively, for a straight line fit to these data. However, the systematic difference in the N_{μ^+}/N_{μ^-} ratio for the DF and DR data sets, as seen in §3.2.2, is also in evidence here.

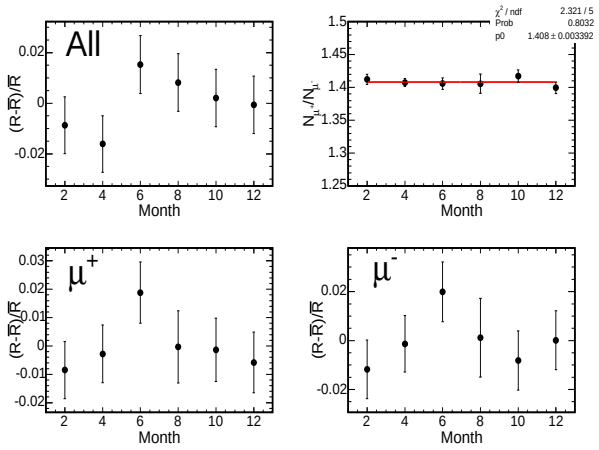

Figure 35. Seasonal Variations in the DF data set averaged over two month intervals. Upper left: total data set, without charge separation cuts; lower left: μ^+; upper right: N_{μ^+}/N_{μ^-} ratio; lower right: μ^-.

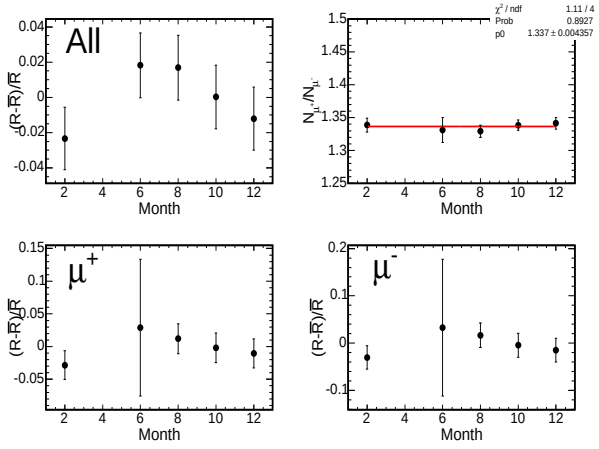

Figure 36. Seasonal Variations in the DR data setaveraged over two month intervals. There are no DF data for months January and February. Upper left: total data set, without charge separation cuts; lower left: μ^+; upper right: N_{μ^+}/N_{μ^-} ratio; lower right: μ^-.

5 Summary

1. Hard cuts are required to minimize systematic effects in charge sign identification for the cosmic muon data sample; after cuts, the Forward (DF) and Reverse (DR) data samples appear to have only very minor systematic differences between them.

2.

6 References

References

[1] Kasahara, S. "A Study of Cosmic Ray Composition in the Knee Region Using Multiple Muon Events in the Soudan2 Detector", Ph.D. Dissertation, University of Minnesota (1997).

[2] Gaisser, T.K. *Cosmic Rays and Particle Physics*, (Cambridge University Press: Cambridge) 1990.

[3] Rebel, B.J. "Neutrino-Induced Muons in the MINOS Far Detector", Ph.D. Dissertation, Indiana University (2004).

[4] Ambrosio, M., *et al. Phys.Rev.D*, **56**, 1407 (1997).

[5] Gaisser, T.K., and Stanev, T. in "Review of Particle Physics" *Phys.Lett.B*, **592**, 248 (2004).

[6] Crouch, M. in *Proc. 20th INt. Cosmic Ray Conf.*, Moscow, **6**, 165 (1987).

[7] Ambrosio, M., *et al. Astropart.Phys.*, **7**, 109, (1997).

[8] Barrett, P.H., *et al. Rev.Mod.Phys.*, **24**, 133 (1952).